A Robust Power Regulation Controller to Enhance Dynamic Performance of Voltage Source Converters

Tiancong Shao, *Member, IEEE*, Pengyu Jia, Peiqi Zheng, Trillion Q. Zheng, *Senior Member, IEEE*, Jiuhe Wang, Hong Li, *Senior Member, IEEE*, Mei Liang, and Xiaochao Zhang

***Abstract*—This paper presents a novel power regulation controller for grid-connected voltage source converter (VSC). The proposed controller is usually applied to achieve smooth active and reactive power dynamics against the variation of parameters. The dynamic performance of grid-connected VSC is sensitive to parameter variation, threatening the safe operation especially when the relative stability is low. Moreover, there is no possibility to modify the dynamic response without the loss of power regulation precision or output voltage and frequency accuracy. In this paper, an improvement in the dynamic response is achieved by introducing feedforward branches into the VSC power regulation controller. Owing to the model reduction mechanism, the VSC provides smooth dynamic response and robustness against the variation of parameters. Simulation and experiment results are presented to prove the effectiveness of this approach, which shows excellent performance as opposed to the conventional controller paradigm.**

***Index Terms*—Dynamic response, power converter, power system control, robustness.**

I. Introduction

AS THE increasing renewable energy penetration [1]–[4], a growing share of power is contributed by distributed generations (DGs), such as energy storage, photovoltaic panels, fuel cells, and wind turbines [5]–[7]. Voltage source converters (VSCs) are widely used as the interfaces between the DGs and grid, because of its excellent flexibility [8]–[10]. The power regulation controller is a critical component in the VSC to balance the active/reactive power injected into the grid, and to keep

Manuscript received January 16, 2019; accepted March 6, 2019. Date of publication March 18, 2019; date of current version September 6, 2019. This work was supported in part by the General Programs of the National Natural Science Foundation of China under Grants 51577010 and 51777012, and in part by the Fundamental Research Funds for the Central Universities under Grant 2017JBM054. Recommended for publication by Associate Editor M. Tavakoli Bina. *(Corresponding author: Tiancong Shao.)*

T. Shao, T. Q. Zheng, H. Li, and X. Zhang are with the School of Electrical Engineering, Beijing Jiaotong University, Beijing 100044, China (e-mail:

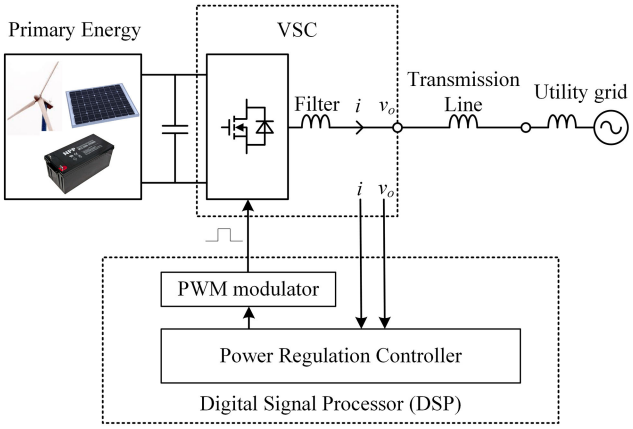

Fig. 1. Grid-connected voltage source converter system.

To fill out this gap, this paper proposes a robust power regulation controller for VSC to enhance the dynamic performance. First, Section II reviews the conventional VSC power regulation controller, summarizes the delay effects that dominate the dynamic response, then reveals the parameter variation's impact on grid-connected VSCs. Second, Section III proposes a VSC power regulation controller based on feedforward branches to enhance the dynamic performance under parameter uncertainty, show the model reduction mechanism for solving this issue, recommends the parameter design process, theoretically proves the enhancement in advance. Finally, Sections IV and V validate the analysis and the proposed controller with time-domain simulation and experiment, respectively.

II. Review of the Conventional VSC Power Regulation Controller

Fig. 1 shows the general diagram of the grid-connected VSC. The primary power generations, such as wind turbines, solar panels, and energy storages, need power electronics to transfer the dc link energy into the grid, where the grid-connected VSC plays an essential role. The VSC converts dc voltage into ac form, and controls the active/reactive power injected into the gird. Inside the VSC, power regulation controller is usually embedded inside the digital signal processor (DSP) of VSC. Based on the measured voltage and current, the power regulation controller regulates the output active/reactive power by the calculated PWM signals. In this case, the interaction of the VSC, the power regulation controller and the power part is essential to the dynamic of grid-connected VSC system.

Fig. 2 shows the scheme of a typical VSC power regulation controller. This VSC controller is based on the cutting-edge VSM called synchronverter, proposed in [15]. Under this controller, VSCs can contribute to the short-term stabilization of the grid frequency. Besides, the system dynamics seen from the grid side will be similar to those of synchronous generators. Thus, the concept of VSM, especially the synchronverter, gained much attention recently.

In Fig. 2, J mimics the moment of inertia of all the parts rotating with the rotor, T_m is the mechanical torque, T_e is the electromagnetic toque, and D_p is a damping factor. For synchronous generators, the rotor speed is maintained by the prime mover, and the damping factor D_p is due to the mechanical friction. The formulas in [15] show that the effect of the frequency-droop control loop is equivalent to a significant increase of the mechanical friction coefficient D_p. In Fig. 2 and later, the constant D_p represents the imaginary mechanical-friction coefficient plus the frequency-drooping coefficient. Similarly, the regulation of reactive power Q flowing out of the VSC can be realized with the voltage drooping coefficient D_q as the ratio of the required change of reactive power to the change of voltage. The resulting signal is then sent into the integrator with a gain $1/K$ to generate $M_f i_f$, which represents the imaginary mutual inductance and rotor excitation current. In Fig. 2, coefficients D_p and D_q ensure the state–state droop control objectives [15] as follows:

$$D_p = \frac{\Delta T_{\text{emax}}}{\triangle \omega_{\text{max}}} \tag{1}$$

$$D_q = \frac{\triangle Q_{\text{max}}}{\triangle V_{\text{max}}} \tag{2}$$

where $\triangle T_{\text{emax}}$ and $\triangle Q_{\text{max}}$ are the maximum virtual torque (proportional to active power) and reactive power deviations that can be delivered by the converter. $\triangle \omega_{\text{max}}$ and $\triangle V_{\text{max}}$ are the maximum angular frequency and output voltage amplitude deviations allowed. Some reference, such as [15], adds minuses before those two equations to address the negative relationship in droop characteristic.

The controller measures the current i and voltage v_o from the power part, calculates the virtual electromagnetic torque τ_e and reactive power q, and then generates the virtual back electromotive force (EMF) e to PWM modular and control power devices. The core calculation equations for torque (proportional to active power), virtual back electromotive force, and reactive power are given in (3)–(5)

$$\tau_e = M_f i_f \left\langle i, \widetilde{\sin}\theta \right\rangle \tag{3}$$

$$e = \omega M_f i_f \widetilde{\sin}\theta \tag{4}$$

$$q = -\omega M_f i_f \left\langle i, \widetilde{\cos}\theta \right\rangle. \tag{5}$$

This paper uses small letters τ_e and q to indicate their instantaneous nature, whereas the power regulation needs average values T_e and Q. The calculation of average value is realized by the average power calculator (APC), which will be introduced in detail in the next section. In the active power loop (see the upper part of Fig. 2), the controller is derived from the swing equation; in the reactive power loop (see the lower part of Fig. 2), the controller is derived from the excitation mechanism. As a result, the VSC will imitate the character of a physical synchronous machine, thus achieve a grid-friendly behavior. VSM-based VSC uses open-loop PWM generation method, the PWM signals are directly generated from e without cascaded voltage and current loops [15]. The frequency and voltage loop time constants

$$\tau_f = J/D_p \tag{6}$$

$$\tau_v = K/(\omega_n D_q) \tag{7}$$

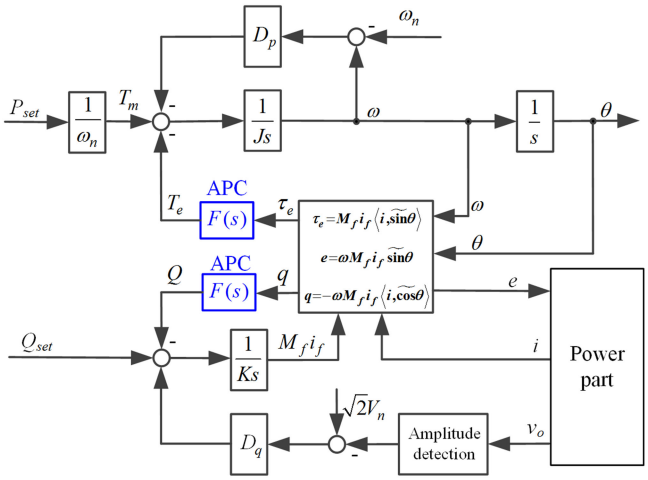

Fig. 2. Conventional VSC power regulation controller.

are introduced in [15]. Those two coefficients evaluate the response speed of frequency and voltage loops, paving the way to understand the mechanism for tuning the parameters J and K in the controller.

Some VSC controllers use cascaded voltage and current loops to make sure the terminal voltage can accurately follow its reference; in fact, refer to the research results in [30], the cascaded voltage and current loops have minor influence on the power regulation, because they have much faster dynamics than the power regulation. Limited by the space, this paper focuses on the power regulation dynamics.

Fig. 3 shows the typical power part of VSC. Both the three-phase and single-phase topologies are given in Fig. 3(a) and (b), respectively. Because of the symmetrical characteristic between the three-phase and single-phase topologies, the reference phase schematic diagram is derived in Fig. 3(c). The VSC is connected to the grid at the point of common coupling (PCC) through an *LC* filter and circuit breaker CB. The power device bridge is powered by dc source $V_{\rm DC}$. The dc source control and energy storage configuration are beyond the scope of this paper, for simplification, in this paper, it is assumed that the dc source control is fast enough and the energy storage is large enough to guarantee $V_{\rm DC}$ has a constant value.

It should be noticed that VSCs in three-phase [15] and single-phase [20] systems have the similar power regulation mechanism. In general, the power regulation controller in Fig. 2 is an expression for both the three-phase and single-phase systems. The symbol $\langle\cdot,\cdot\rangle$ denotes the conventional inner product [15]. For a three-phase system, i and θ represent 3×1 matrices: $i=[i_a,i_b,i_c]^T$ and $\theta=[\theta_a,\theta_b,\theta_c]^T$; in the meantime, matrix $\widetilde{\sin\theta}=[\sin\theta_a,\sin\theta_b,\sin\theta_c]^T$ and matrix $\widetilde{\cos\theta}=[\cos\theta_a,\cos\theta_b,\cos\theta_c]^T$; for a single-phase system, i and θ represent 1×1 matrices: $i=[i_a]$ and $\theta=[\theta_a]$, and the matrix $\widetilde{\sin\theta}=[\sin\theta_a]$ and matrix $\widetilde{\cos\theta}=[\cos\theta_a]$.

The *LC* filter is composed of the filter inductor L_s and filter capacitor C_f. The line-frequency-average based modeling process will not be influenced by the filter capacitor C_f as it only influences the high-frequency signals [31]. Z_s denotes the converter filter inductor impedance, which also mimics the synchronous generator stator inductor and its inner resistance. In this paper, the grid voltage is replaced by an ideal voltage source in series connection with an equivalent grid impedance, according to the Thevenin theorem. The ideal voltage source has constant amplitude and frequency. Z_g denotes the grid impedance and transmission line (as well as transformer, if needed) impedance. The converter supplies power through the ac-side impedance. In this paper, the term ac-side impedance Z denotes the sum of Z_s and Z_g, i.e., $Z=Z_s+Z_g$.

The following part of this section will introduce APC bandwidth ω_b and power loop time constants τ_p, τ_q to evaluate the delay effect, and then show their influence on the dynamic performance.

A. *Delay Effect of the APC*

The APC is the element in VSC power regulation controller to calculate the average value from the instantaneous value. The output instantaneous real power p and reactive power q, with the superposition oscillating portions $\tilde{p}$ and $\tilde{q}$, are given as

$$p=\langle i,e\rangle=\frac{2}{T_{\rm line}}\int_{T_{\rm line}/2}\langle i,e\rangle\,dt+\tilde{p}$$

$$q=\langle i,e_q\rangle=\frac{2}{T_{\rm line}}\int_{T_{\rm line}/2}\langle i,e_q\rangle\,dt+\tilde{q}$$

where e_q has the same amplitude as e but with a phase delayed from that of e by $\pi/2$, and $T_{\rm line}$ represents the line period. For a three-phase VSC supplying power to a balanced or ideal three-phase voltage source, the instantaneous power coincide with the line-frequency-averaged power. However, in an unbalanced three-phase system or a single-phase system, the output instantaneous powers contain superposition oscillating portions $\tilde{p}$ and $\tilde{q}$ [32]. Hence, APC is essential for VSC and its delay effect is inevitable.

The bandwidth describes the delay effect. First-order low-pass filter is the most common APC. Hence, the transfer function of APC is given as

$$F(s)=\frac{\omega_b}{s+\omega_b}$$

where ω_b denotes the bandwidth of APC, which is defined as the first angular frequency where the gain drops below 70.79% (-3 dB) [33]. Fig. 4 shows the magnitude of $F(s)$ with different values of bandwidth ω_b, the increase of bandwidth ω_b leads to the increase of magnitude. While, to precisely regulate the power, voltage and frequency, the magnitude at twice the line frequency $|F(j\cdot 2\omega_l)|$ should be small enough. Hence, the APC bandwidth has an upper limit. For example, in a 50-Hz system, for an APC with magnitude smaller than -26.4 dB, the bandwidth should be smaller than 30 rad/s, i.e., $\omega_b<30$ (rad/s). The APC bandwidth ω_b has a relatively large degree of freedom for design. However, the APC with a smaller bandwidth ω_b usually has a slower response. That means the attenuation function also introduces a delay effect for VSC, which would impact the dynamic response and relative stability.

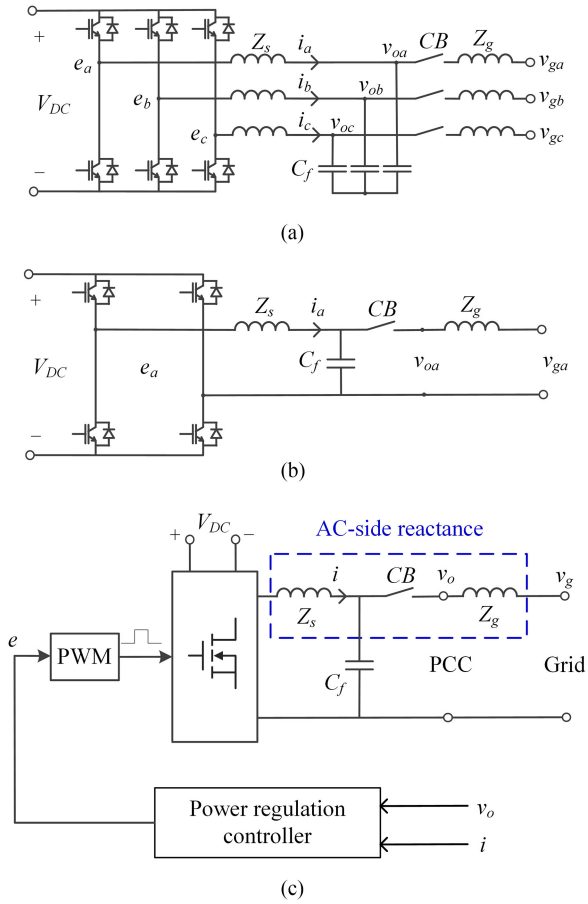

Fig. 3. VSC power part: (a) three-phase, (b) single-phase, and (c) reference phase schematic diagram.

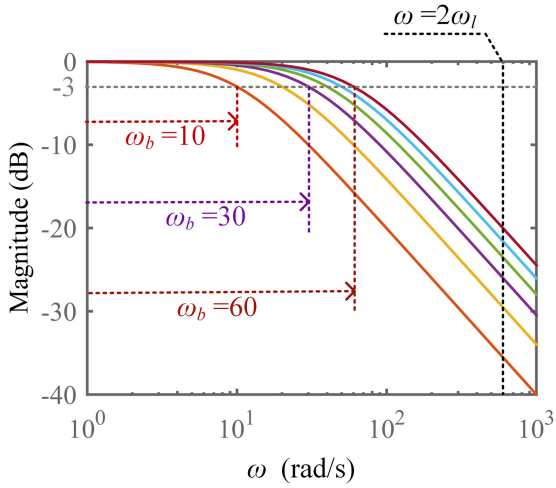

Fig. 4. Average power calculator bandwidth ω_b (rad/s) and its magnitude (dB) at twice the line frequency.

B. Delay Effect of the AC-Side Reactance

This part introduces power loop time constants to describe the delay effect of ac-side reactance. With the assistant of power loop time constants, the analysis below would base on the rated condition and per-unit values. Hence, the results generated are appropriate for VSCs under different power level and voltage level. Dynamic characteristics of a power system can be obtained by small-signal analysis using linear techniques [34]. VSC connected with the grid can be analyzed in the same way [11]. The phasor representations of the sinusoidal voltage and current can be used to calculate the active and reactive powers [35].

The phasor representation is shown in Fig. 5. It is given in the single-phase form, in the three-phase system, it represents the reference phase. Phasor $\dot{E} = E/\sqrt{2}\angle\delta$ and $\dot{V}_g = V_g/\sqrt{2}\angle 0^\circ$ represent the virtual back EMF e and the grid voltage v_g, respectively. E and ω represent, respectively, the virtual back EMF amplitude and angular frequency, and V_g and ω_g represent the grid voltage amplitude and angular frequency, respectively. Then, the expression of power angular δ can be given as

$$\delta = \int (\omega - \omega_g) dt. \tag{8}$$

The ac-side impedance is represented by $Z = Z_s + Z_g$ and X denotes the inductive component. Hence, the phasor of the output current can be given as

$$\dot{I} = \frac{\dot{E} - \dot{V}_g}{Z}.$$

In this paper, it is assumed that the ac-side impedance Z is mainly inductive with the reactance represented by X. If not, a virtual inductor can be introduced to be in series with it through the control strategy, and thus making the impedance to be inductive [36]. As a result, the phasor of output current can be rewritten as

$$\dot{I} = \frac{\dot{E} - \dot{V}_g}{jX}.$$

For a system with N-phase system, i.e., $N = 3$ and $N = 1$ correspond to three-phase and single-phase conditions, respectively, the output complex power of the converter can be expressed as

$$\begin{aligned}\dot{S} = N\dot{E}\dot{I}^\star &= \frac{N}{2X} EV_g \sin\delta + j\frac{N}{2X}(E^2 - EV_g\cos\delta) \\ &= P + jQ\end{aligned}$$

where the line-frequency-averaged active power P and reactive power Q transferred from the converter to the grid can be written as follows:

$$P = \frac{N}{2X} EV_g \sin\delta \tag{9}$$

$$Q = \frac{N}{2X}(E^2 - EV_g\cos\delta). \tag{10}$$

It should be noticed that the model to be derived, based on (9) and (10), is only valid for the frequency range that is lower than the line frequency [37]. Nevertheless, it is enough for system analysis [31]. In this paper, the term ac-side reactance denotes the total reactance the VSC power goes through, as shown in the line-frequency-averaged average power calculation in (9) and (10).

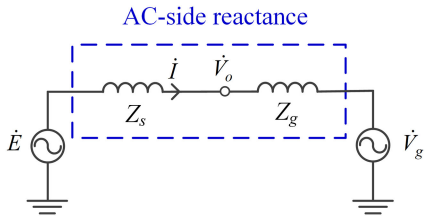

Fig. 5. System phasor representation.

The VSC output frequency ω and output voltage E will be controlled by the power regulation controller given in Fig. 2, from which the time-domain differential equations are obtained

$$J\frac{d\omega}{dt} = T_m - T_e - D_p(\omega - \omega_n)$$

$$K\frac{dM_f i_f}{dt} = Q_{\text{sel}} - Q + D_q(\sqrt{2}V_n - \sqrt{2}V_o)$$

where ω_n is the rated angular frequency. In the neighborhood of rated angular frequency ω_n, the above-stated equations transform into

$$J\frac{d\omega}{dt} = \frac{P_{\text{sel}} - P}{\omega_n} - D_p(\omega - \omega_n) \tag{11}$$

$$\frac{K}{\omega_n}\frac{dE}{dt} = Q_{\text{sel}} - Q + D_q(\sqrt{2}V_n - \sqrt{2}V_o). \tag{12}$$

Consider the small-signal disturbance near the equilibrium state (δ_e, E_e, V_e), linearize (8)–(12)

$$\triangle\delta = \frac{1}{s}\triangle\omega \tag{13}$$

$$\triangle P = K_{pd}\triangle\delta + K_{pe}\triangle E \tag{14}$$

$$\triangle Q = K_{qd}\triangle\delta + K_{qe}\triangle E \tag{15}$$

$$\triangle\omega = -\frac{1}{J\omega_n s + D_p\omega_n}\triangle P \tag{16}$$

$$\triangle E = -\frac{\omega_n}{Ks}\triangle Q \tag{17}$$

where the proportional constants in active/reactive power loops, $K_{pd} = \frac{\partial P}{\partial\delta}\,|_e$, $K_{pe} = \frac{\partial P}{\partial E}\,|_e$, $K_{qd} = \frac{\partial Q}{\partial\delta}\,|_e$, and $K_{qe} = \frac{\partial Q}{\partial E}\,|_e$, are the partial differential at the equilibrium point.

Usually, the nominal value of δ is small enough so the coupling effect between active power loop and reactive power loop has a minor influence on the system [31]. Hence, $\triangle P$ is mainly impacted by $\triangle\delta$ and $\triangle Q$ is mainly impacted by $\triangle E$. As a result, without losing too much accuracy, the active power and reactive power loops can be analyzed ignoring the coupling. The small-signal model block diagram of the VSC is given in Fig. 6.

Considering that the equilibrium point value is approximately equal to the nominal value [11], [31], K_{pd} and K_{qe} can be expressed as

$$K_{pd} = \frac{\partial P}{\partial\delta}\,|_e \approx \frac{NV_n^2}{X}$$

$$K_{qe} = \frac{\partial Q}{\partial E}\,|_e \approx \frac{\sqrt{2}NV_n}{2X}.$$

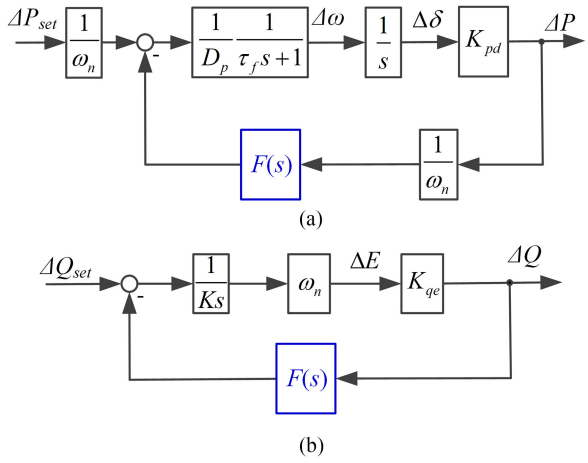

Fig. 6. VSC with the conventional controller, small-signal model block diagrams. (a) Active power loop. (b) Reactive power loop.

Assume the base voltage is chosen as the rms phase voltage V_n and the base power is chosen as the rated power S_n. Then, the base impedance is

$$Z_{\text{base}} = NV_n^2/S_n$$

and the ac-side reactance

$$X = X_{\text{pu}}Z_{\text{base}} = X_{\text{pu}}NV_n^2/S_n$$

where X_{pu} is the per-unit ac-side reactance. Then, K_{pd} and K_{qe} can be rewritten in the per-unit form

$$K_{pd} = \frac{S_n}{X_{\text{pu}}} \tag{18}$$

$$K_{qe} = \frac{S_n}{\sqrt{2}V_n X_{\text{pu}}}. \tag{19}$$

In order to evaluate the delay effect of reactance, this part assumes that the other elements in the loops has no delay, i.e., $\tau_f \approx 0$ and APC bandwidth $\omega_b \to \infty$. Hence, the transfer functions can be derived from Fig. 6

$$\frac{\triangle P}{\triangle P_{\text{sel}}} = \frac{1}{\tau_p s + 1}$$

$$\frac{\triangle Q}{\triangle Q_{\text{sel}}} = \frac{1}{\tau_q s + 1}$$

where the time constants of active/reactive power loop are given as

$$\tau_p = \frac{\omega_n D_p}{K_{pd}} \tag{20}$$

$$\tau_q = \frac{K}{\omega_n K_{qe}}. \tag{21}$$

The power loop time constants evaluate the active/reactive power loop response speed. Next, this paper will show the relationship between ac-side reactance and power loop time constants. D_p and D_q are the droop factors, which are given in (1)

and (2) , can be rewritten as

$$D_p = \frac{S_n/\omega_n}{2\pi f_n \alpha} \tag{22}$$

$$D_q = \frac{S_n}{\sqrt{2}V_n \beta} \tag{23}$$

where α and β are the frequency regulation factor and voltage regulation factor, respectively. Equation (22) means that a frequency drop of α (from nominal frequency) causes the torque (hence, the active power) to increase by 100% (from nominal apparent power), similarly, (23) means that a voltage drop of β (from nominal voltage) causes the reactive power to increase by 100% (from nominal apparent power). Taking the above-stated equations into account, (20) and (21) can be rewritten in the per-unit form

$$\tau_p = \frac{X_{\text{pu}}}{\omega_n \alpha} \tag{24}$$

$$\tau_q = \frac{\tau_v X_{\text{pu}}}{\beta}. \tag{25}$$

From (24) and (25), it is clear that the power loop time constants directly proportional to ac-side reactance represented by X_{pu}. The active/reactive power loops with a larger per-unit ac-side reactance usually has a slower response. That means the ac-side reactance delays the response of active/reactive power loops.

C. Dynamic Response Under Parameter Variation

It should be noticed that the delay elements mentioned above interacts with each other and strongly impacts the dynamic process and relative stability. The delay elements have two parts: APC and ac-side reactance (the sum of filter reactance, line reactance, and grid inner reactance). This part will introduce how the APC bandwidth ω_b and per-unit ac-side reactance X_{pu} impact on VSC dynamic response.

The regulation mechanism of the active power (torque) shown in the upper part of Fig. 2(a) has a nested structure where the inner loop is the frequency loop and the outer loop is the more complex active power loop (with the feedback coming from the current i via the torque T_e). Fig. 6(a) shows the active power loop small-signal model whose characteristic equation can be obtained

$$\frac{\tau_p \tau_f}{\omega_b} s^3 + \tau_p \left(\tau_f + \frac{1}{\omega_b}\right) s^2 + \tau_p s + 1 = 0. \tag{26}$$

Because τ_f, τ_p, and $1/\omega_b$ are far smaller than 1, the third-order coefficient is far smaller than the rest coefficients. Hence, the above-mentioned third-order system can be simplified as a second-order system with a characteristic equation

$$\tau_p \left(\tau_f + \frac{1}{\omega_b}\right) s^2 + \tau_p s + 1 = 0. \tag{27}$$

Rewrite the above-stated equation into the standard form of second-order system

$$s^2 + \frac{1}{\tau_f + 1/\omega_b} s + \frac{1}{\tau_p(\tau_f + 1/\omega_b)} = 0. \tag{28}$$

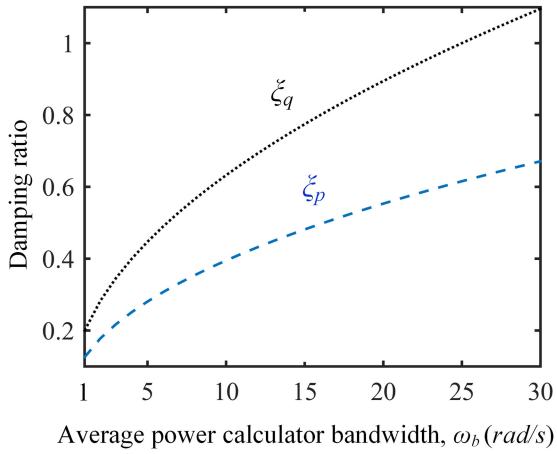

Fig. 7. VSC with conventional controller. Damping ratio varies with the APC bandwidth ω_b.

Equation (28) corresponds to the dominate poles of the active power loop in Fig. 6(a). From (28), the damping ratio of active power loop is obtained

$$\xi_p = \frac{1}{2}\sqrt{\frac{\tau_p}{\tau_f + 1/\omega_b}}. \tag{29}$$

Similarly, the characteristic equation of the reactive power loop shown in Fig. 6(b) is

$$s^2 + \omega_b s + \frac{\omega_b}{\tau_q} = 0. \tag{30}$$

From (30), the damping ratio of reactive power loop is obtained

$$\xi_q = \frac{1}{2}\sqrt{\tau_q \omega_b}. \tag{31}$$

Substituting (24) and (25) in (29) and (31), they result

$$\xi_p = \frac{1}{2}\sqrt{\frac{X_{\text{pu}}}{\omega_n \alpha} \cdot \frac{1}{1/\omega_b + \tau_f}} \tag{32}$$

$$\xi_q = \frac{1}{2}\sqrt{\frac{\tau_v X_{\text{pu}} \omega_b}{\beta}} \tag{33}$$

where α and β are designed by grid code corresponding with droop factors. ω_n is the nominal angular frequency. τ_f and τ_v are the time constants of frequency loop and voltage loop, whose design rules have already settled in [15]. They are designed to have fast response, and the frequency/voltage loops are faster than the active/reactive loops, i.e., $\tau_f < \tau_p$ and $\tau_v < \tau_q$ [15]. Hence, the damping ratios of active/reactive power loops, ξ_p and ξ_q, are determined by the per-unit ac-side reactance X_{pu} and the APC bandwidth ω_b.

Take a VSC in 50-Hz system as an example to calculate the damping ratio by (32) and (33), in this example, the frequency/voltage regulation factors are $\alpha = 0.5\%$, $\beta = 5\%$, the control parameters are $\tau_f = 0.002s$, $\tau_v = 0.08s$. Fig. 7 shows the variation of damping ratio following with the change of APC bandwidth. As it is mentioned above, the APC bandwidth has a relatively wide choice range. In the figure, the APC bandwidth

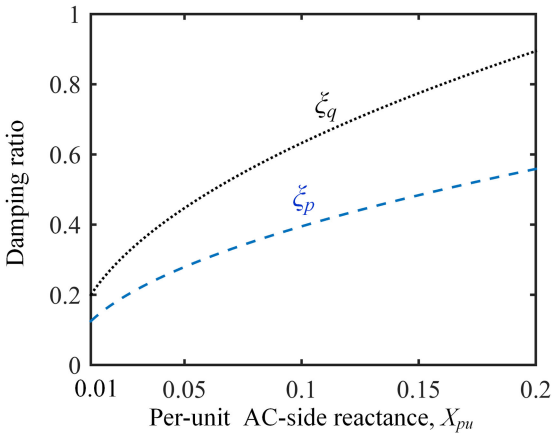

Fig. 8. VSC with conventional controller. Damping ratio varies with the per-unit ac-side reactance X_{pu}.

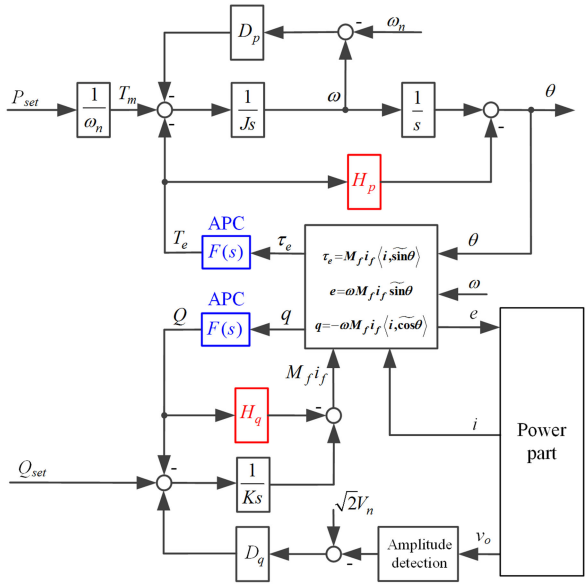

Fig. 9. Proposed VSC power regulation controller. Robust controller to improve dynamic performance.

ω_b changes from 1 to 30 rad/s, where the per-unit ac-side reactance $X_{\text{pu}} = 0.1$. While ω_b changes from 1 to 30, ξ_p changes from 0.13 to 0.67 and ξ_q changes from 0.21 to 1.10. In brief, the decrease of APC bandwidth leads to the decrease of damping ratio.

Similarly, Fig. 8 shows that the change of ac-side reactance influences the damping ratios of VSC, resulting in oscillation of active and reactive power dynamics. In modern power system, a very important part of the ac-side reactance is the synchronous reactance. The synchronous reactance of synchronous generator varies diversely with the type. For hydraulic units it is 0.6–1.5, whereas for thermal units it is 1–2.3. However, in VSC condition, the filter inductor is designed to restrain high-frequency harmonic, usually kHz level, hence, the ac-side reactance is much lower than synchronous generators, such as: $X_{\text{pu}} = 0.0655$ and 0.0437 in the VSCs of [15] and [38], respectively. Hence, the variation range of X_{pu} is chosen to be 0.01–0.2 in Fig. 8, which shows the damping ratio change and the average bandwidth is $\omega_b = 10$ rad/s. While X_{pu} changes from 0.01 to 0.2, ξ_p changes from 0.12 to 0.56 and ξ_q changes from 0.2 to 0.88. In brief, the decrease of ac-side reactance leads to the decrease of damping ratio.

In conclusion, the delay effect comes from both the power regulation controller and the power part, it has two aspects. First, the delay effect contributed by the APC in the power regulation controller where the APC is originally introduced to attenuate the instantaneous power oscillating portion [12], [32], [39]. Second, the delay effect contributed by the ac-side reactance in the power part, which includes VSC filter reactance, transmission line reactance, and grid reactance [11], [40], [41]. On one hand, APC bandwidth and ac-side reactance have a relatively large degree of freedom for design, which is determined by the application conditions (such as grid impedance, transmission line parameters, filter requirement, converter's dc voltage, switching frequency, unbalance coefficient, etc.) [42]–[44]. On the other hand, APC bandwidth and ac-side reactance have uncertainty, this is because of the error between the mathematical and actual value of reactance in engineering applications [45], [46]. It should be noticed that mismatched parameters might lead to low relative stability condition, in this case, the disturbance of parameters would cause significant damage.

The mismatch between APC bandwidth and ac-side reactance would lead to the lack of damping ratio. As a result, the system would tend to oscillate. Moreover, there is no possibility to modify the dynamic response without the loss of power regulation precision or output voltage and frequency accuracy. The robustness against parameter variation needs to be improved.

III. Proposed Controller and the Robustness Improvement

In this paper, a novel VSC power regulation controller is proposed to overcome the above-mentioned limitations that could be appropriate for high-performance power electronics interface. By adding feedforward branches with gain factors H_p and H_q, this paper gives a novel VSC power regulation controller, as shown in Fig. 9(a). Next parts would show the modifications and demonstrate the feasibility of the proposed optimization. The proposed optimization is easy to realize, only by adding two feedforward branches to the controller, the power part remains, as shown in Fig. 2(b). With the model reduction mechanism, the active/reactive power loops are modified from high-order systems into first-order systems. Finally, the delay effect of APC is offset while the attenuation function remains. The model reduction based parameter design method is described in this section. Furthermore, to show the robustness improvement, this section also compares the relative stability of VSCs based on conventional controller and the proposed controller.

A. Model Reduction

This part will show the small-signal model at first. Fig. 10 shows the small-signal model of the proposed controller. Here, the factors K_{pd} and K_{qe}, shown in (18) and (19), are obtained

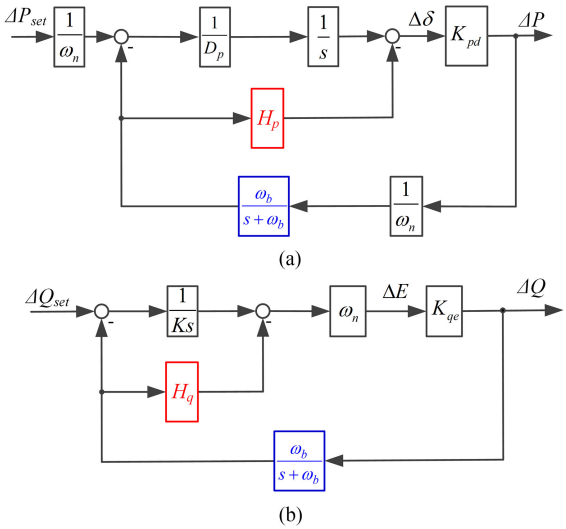

Fig. 10. VSC with the proposed controller, small-signal model block diagrams. (a) Active power loop. (b) Reactive power loop.

by the same linearization method as mentioned above. The other parameters besides newly added H_p and H_q, comply with the same design rules of conventional VSC controller, i.e., to design the frequency loop time constant $\tau_f = J/D_p$ and voltage loop time constant $\tau_v = K/(\omega_n D_q)$ [15]. The frequency loop should be fast enough to establish frequency, $\tau_f \ll 1/\omega_b$, $\tau_f \ll \tau_p$, and $\tau_f \ll 1$. For simplification, it is approximated that

$$\frac{1}{D_p} \cdot \frac{1}{\tau_f s + 1} \approx \frac{1}{D_p}. \tag{34}$$

The values of H_p and H_q are designed to realize the model reduction. Fig. 10(a) illustrates the active power loop of the proposed controller. Furthermore, based on Fig. 10(a), the characteristic equation of the active power loop can be derived as

$$1 + \frac{K_{pd}}{\omega_n D_p s} \frac{D_p H_p s + 1}{1/\omega_b s + 1} = 1 + \frac{1}{\tau_p s} \frac{D_p H_p s + 1}{1/\omega_b s + 1} = 0.$$

Hence, the feedforward branch provides a new degree of freedom to reconfigure the characteristic equation above. The $D_p H_p s + 1$ portion offsets the APC portion $\frac{1}{1/\omega_b s+1}$ when $H_p = \frac{1}{D_p \omega_b}$. On condition that $H_p = \frac{1}{D_p \omega_b}$, the characteristic equation of the active power loop is reconfigured to be

$$1 + \frac{1}{\tau_p s} = 0. \tag{35}$$

Obviously, the newly reconfigured characteristic equation is a first-order system. Similarly, based on Fig. 10(b), the characteristic equation of the reactive power loop can be derived as

$$1 + \frac{\omega_n K_{qe}}{K s} \frac{K H_q s + 1}{1/\omega_b s + 1} = 1 + \frac{1}{\tau_q s} \frac{K H_q s + 1}{1/\omega_b s + 1} = 0.$$

The $K H_q s + 1$ portion offsets the APC portion $\frac{1}{1/\omega_b s+1}$ when $H_q = \frac{1}{K \omega_b}$. Furthermore, the characteristic equation of the reactive power loop is reconfigured to be

$$1 + \frac{1}{\tau_q s} = 0. \tag{36}$$

Then the reactive power loop is also reduced to a first-order system. After the equivalent conversion of block diagrams in Fig. 10 and design $H_p = \frac{1}{D_p \omega_b}$ and $H_q = \frac{1}{K \omega_b}$, the simplified small-signal model can be obtained in Fig. 11. Equations (35) and (36) also show that the each loop only has one characteristic root. Meanwhile, characteristic equations, i.e., (27) and (30), show that VSC controlled by conventional method has at least two poles in each loop. Hence, the newly introduced feedforward branches reduced the system order from second order to first order.

In a word, the feedforward branch provides a new degree of freedom to reconfigure the active/reactive power loops' characteristic equations. By designing feedforward branch gains to be

$$H_p = \frac{1}{D_p \omega_b} \tag{37}$$

$$H_q = \frac{1}{K \omega_b} \tag{38}$$

the VSC realize the model reduction. Next part will show the optimization result of robustness after using model reduction mechanism.

B. Design Methodology

This part summarizes the following parameter design process to properly select the coefficients of the proposed controller in Fig. 9.

1) Coefficients D_p and D_q can be designed, as in the conventional VSC power regulation control method, to ensure state-state droop control objectives, chosen by the designer considering about the tradeoff between the power sharing accuracy and the frequency and amplitude deviation, fixed by tuning parameters α and β, see (22) and (23).

2) Coefficients J and K can be designed, as in the conventional VSC power regulation control method, to adjust the transient response rate, chosen by the designer considering about the tradeoff between response speed and system stability, fixed by tuning parameters τ_f and τ_v in (6) and (7).

3) Coefficients H_p and H_q are designed to ensure the dynamic improvement with robustness, chosen by the designer considering about the model reduction, see (37) and (38).

C. Dynamic Response Improvement

By comparing the closed-loop frequency characteristic, this part will demonstrate the dynamic response improvement. Before showing the frequency characteristic, this part derives the closed-loop transfer functions of active/reactive power loops. The closed-loop transfer functions of VSC with the conventional controller can be derived from Fig. 6. In the active power loop, taking the simplification in (34) into consideration, the transfer function from the active power set point $\triangle P_{\text{sel}}$ to output active power $\triangle P$ is

$$\frac{\triangle P}{\triangle P_{\text{sel}}} = \frac{1/\omega_b \cdot s + 1}{\tau_p/\omega_b \cdot s^2 + \tau_p \cdot s + 1}. \tag{39}$$

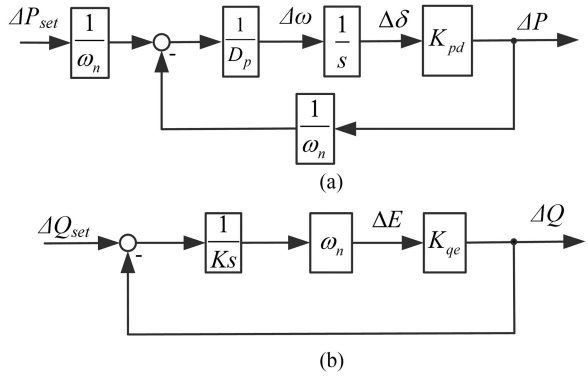

Fig. 11. VSC with the proposed controller, small-signal model after equivalent conversion. (a) Active power loop. (b) Reactive power loop.

In the reactive power loop, the transfer function from the reactive power set point $\triangle Q_{\text{sel}}$ to output reactive power $\triangle Q$ is

$$\frac{\triangle Q}{\triangle Q_{\text{sel}}} = \frac{1/\omega_b \cdot s + 1}{\tau_q/\omega_b \cdot s^2 + \tau_q \cdot s + 1} \tag{40}$$

where the expressions of power loop time constants τ_p, τ_q are given in (20) and (21), respectively. The closed-loop transfer functions of the VSC under the robust optimized controller can be derived from Fig. 11. In the active power loop, the transfer function from the active power set point $\triangle P_{\text{sel}}$ to output active power $\triangle P$ is

$$\frac{\triangle P}{\triangle P_{\text{sel}}} = \frac{1}{\tau_p \cdot s + 1}. \tag{41}$$

In the reactive power loop, the transfer function from the reactive power set point $\triangle Q_{\text{sel}}$ to output reactive power $\triangle Q$ is

$$\frac{\triangle Q}{\triangle Q_{\text{sel}}} = \frac{1}{\tau_q \cdot s + 1} \tag{42}$$

where the expressions of power loop time constants τ_p, τ_q are also given in (20) and (21). Based on (39)–(42), the following gives the frequency characteristic.

In the example used for analysis, the nominal frequency is 50 Hz, the frequency/voltage regulation factors are $\alpha = 0.5\%$, $\beta = 5\%$, the control parameters are $\tau_f = 0.002s$, $\tau_v = 0.08s$. Fig. 12 illustrates the active power loop frequency characteristics, given in (39) and (41), respectively. Fig. 12(a) shows the bode diagram of $\triangle P/\triangle P_{\text{sel}}$ with different values of APC bandwidth ω_b, where the left column represents the VSC controlled by the conventional method (denoted as "Conventional controller") and the right column represents the VSC controlled by the proposed controller (denoted as "Proposed controller"). The curves of the conventional controller contain resonance phenomenon, as ω_b approaches from 30 to 1, the resonant frequency decreases, but the resonant peak increases, indicating a deteriorate dynamic response. Nevertheless, under the proposed controller, the curves of VSC have no resonance phenomenon; the curves represent a standard first-order frequency characteristic, inherited from the model reduction mechanism. It should be noticed that the value of τ_p, refer to (24), is not influenced by ω_b, hence, the curves on the right-hand side overlap each other

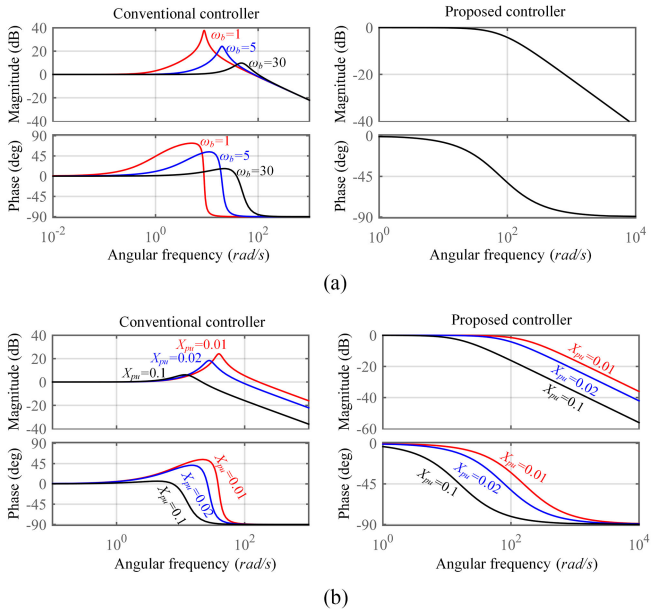

Fig. 12. Closed-loop frequency characteristic $\frac{\triangle P}{\triangle P_{\text{sel}}}$. (a) $\omega_b = 1, 5, 30$, when $X_{\text{pu}} = 0.02$. (b) $X_{\text{pu}} = 0.01, 0.02, 0.1$, when $\omega_b = 10$.

even with the different value of ω_b. Fig. 12(b) shows the bode diagram of $\triangle P/\triangle P_{\text{sel}}$ with different values of per-unit ac-side reactance X_{pu}. The curves of conventional controller contain resonance phenomenon, as X_{pu} decreases from 0.1 to 0.01, both the resonant frequency and the resonant peak increases, indicating a deteriorate dynamic response. Nevertheless, inherited from the model reduction mechanism, the curves of VSC controlled by the proposed controller have no resonance phenomenon. It should be noticed that the power loop time constant τ_p is proportional to X_{pu}, refer to (24); hence, as X_{pu} decrease, the active power loop response gets faster.

Fig. 13 illustrates the reactive power loop frequency characteristics, given in (40) and (42), respectively. Similar to the analysis mentioned above of active power loop frequency characteristics, the curves of VSC with conventional controller contain resonance phenomenon, meanwhile, curves generated by the VSC controlled by the proposed controller show smooth standard first-order frequency characteristic. As ω_b or X_{pu} decreases, the resonant peak increases.

In a word, the optimized controller can remove the resonance in closed-loop frequency characteristic, hence, the dynamic response would be smooth and no oscillation.

D. Robustness Against Parameter Variation

This part will demonstrate the optimization of the robustness against the parametric uncertainty of delay elements. Phase margin indicates the system relative stability, describes the tendency to oscillate during the system's damped response to an input change. In the frequency-response approach to control system design, phase margin are used to take care of the parametric uncertainty [33]. The concept of phase margin is introduced for quantitative comparison.

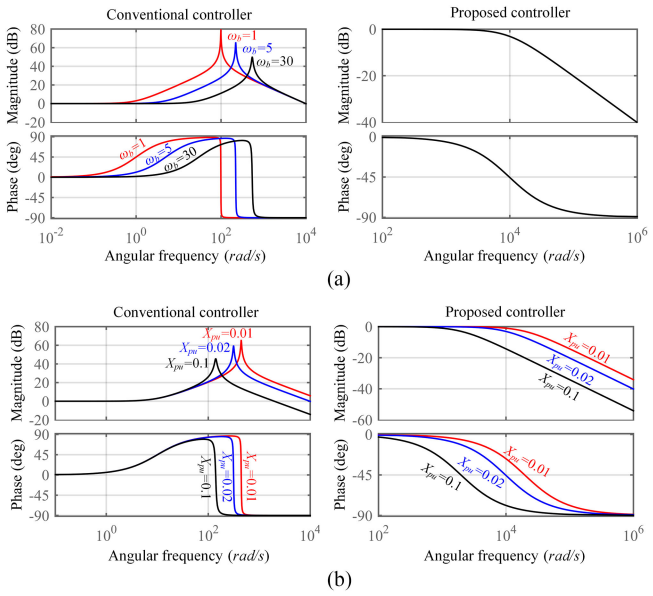

Fig. 13. Closed-loop frequency characteristic $\frac{\triangle Q}{\triangle Q_{\text{sel}}}$. (a) $\omega_b = 1, 5, 30$, when $X_{\text{pu}} = 0.02$. (b) $X_{\text{pu}} = 0.01, 0.02, 0.1$, when $\omega_b = 10$.

For the proposed controller, the loop gains of active/reactive loop can be derived from Fig. 11(a) and (b), respectively

$$G_{Fp}(s) = \frac{1}{\tau_p} \cdot \frac{1}{s} \tag{43}$$

$$G_{Fq}(s) = \frac{1}{\tau_q} \cdot \frac{1}{s}. \tag{44}$$

The phase margins can be calculated from the loop gains shown in (43) and (44), and both equal to 90°. The variation of ω_b and X_{pu} will not change the phase margins .

For the conventional controller, the active/reactive loop gains can be derived from Fig. 6(a) and (b), respectively

$$G_{Cp}(s) = \frac{1}{\tau_p} \cdot \frac{1}{s} \cdot \frac{1}{\frac{1}{\omega_b}s + 1} \tag{45}$$

$$G_{Cq}(s) = \frac{1}{\tau_q} \cdot \frac{1}{s} \cdot \frac{1}{\frac{1}{\omega_b}s + 1} \tag{46}$$

where the simplification in (34) is taken into consideration. The phase margins of VSC with conventional controller is influenced by the APC bandwidth ω_b and the per-unit ac-side reactance X_{pu}, hence, the phase margins will change along with the ac-side reactance change. The analytical form of phase margins is complicated, hence, to facilitate understanding, Fig. 14 illustrates the relative stability with different ω_b and X_{pu}, where the nominal frequency is 50 Hz, the frequency/voltage regulation factors are $\alpha = 0.5\%$, $\beta = 5\%$, the control parameters are $\tau_f = 0.002$ s, $\tau_v = 0.08$ s.

Fig. 14(a) shows the phase margins with a different value of APC bandwidth ω_b where the per-unit ac-side reactance $X_{\text{pu}} = 0.1$. The phase margins of the conventional controller decreases along with the decrease of APC bandwidth ω_b. Following with $\omega_b$decreases from 30 to 1 rad/s, the active power loop phase margin of VSC with the conventional controller decreases from 63° to 14°; the reactive power loop phase margin decreases from 78° to 22°. However, the phase margins of VSC with the proposed controller are both equal to 90° and stay constant against the variation of ω_b. Hence, VSC with the proposed controller has stronger robustness against the variation of APC bandwidth. Fig. 14(b) shows the phase margins with a different value of per-unit ac-side reactance X_{pu} where the APC bandwidth is $\omega_b = 10$ rad/s. The phase margins of VSC with the conventional controller decreases along with the decrease of per-unit ac-side reactance X_{pu}. Following with X_{pu} decreases from 0.2 to 0.01, the active power loop phase margin of conventional controller decreases from 56° to 10°; the reactive power loop phase margin decreases from 73° to 22°. However, the phase margins of the VSC with proposed controller are both equal to 90° and stay constant against the variation of X_{pu}. Hence, VSC with the proposed controller has stronger robustness against the variation of AC-side reactance, and the relative stability independent with delay parameters. In brief, the proposed controller can optimize the VSC dynamic response and robustness against the variation parameters.

TABLE I
PARAMETERS OF THE SINGLE-PHASE VSC

Parameters	Values	Parameters	Values
τ_f	0.002 s	τ_v	0.08 s
α	0.5 %	β	5 %
V_{DC}	42 V	Nominal voltage	12 V
Nominal frequency	50 Hz	Nominal apparent power	100 VA

IV. Simulation Results

The ideas described earlier have been verified with time-domain simulations. In this part, the grid-connected VSC operated in single-phase system and three-phase system with different rated power are investigated, where the single-phase converter worked with relatively low voltages. The reason for this is to make the simulation results comparable with the experimental results to be given in the next section. However, the proposed optimization method should work for high voltage and high power as well, as given in the three-phase VSC simulation.

A. Single-Phase System

The parameters of the converter used in the simulation is given in Table I. Here, $D_p = 0.2026$, which means that a frequency drop of 0.5% causes the torque (hence, the power) to increase by 100% (from nominal apparent power), i.e. $\alpha = 0.5\%$. $D_q = 117.88$, which means that a voltage drop of 5% causes the reactive power to increase by 100% (from nominal apparent power), i.e., $\beta = 5\%$. Control parameters τ_f and τ_v are designed based on the recommendation in [15].

In Figs. 15 and 16, both the simulation result and the small-signal calculation result are given. The simulation is carried out in MATLAB R2014b with Simulink. The solver used in the simulation was ode23tb with a relative tolerance of 10^{-3} and a maximum step size of 0.2 ms. The power part is shown in

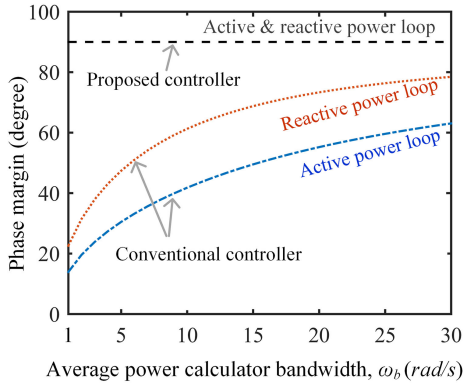

(a)

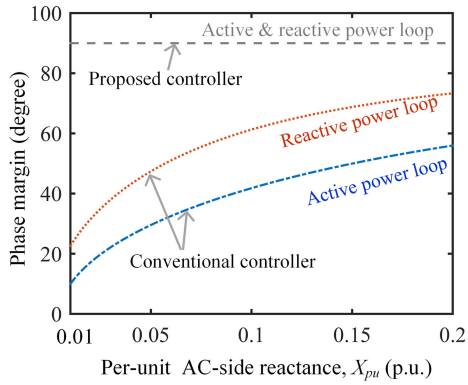

(b)

Fig. 14. Robustness against the variation of parameters. (a) Variation of ω_b. (b) Variation of X_{pu}.

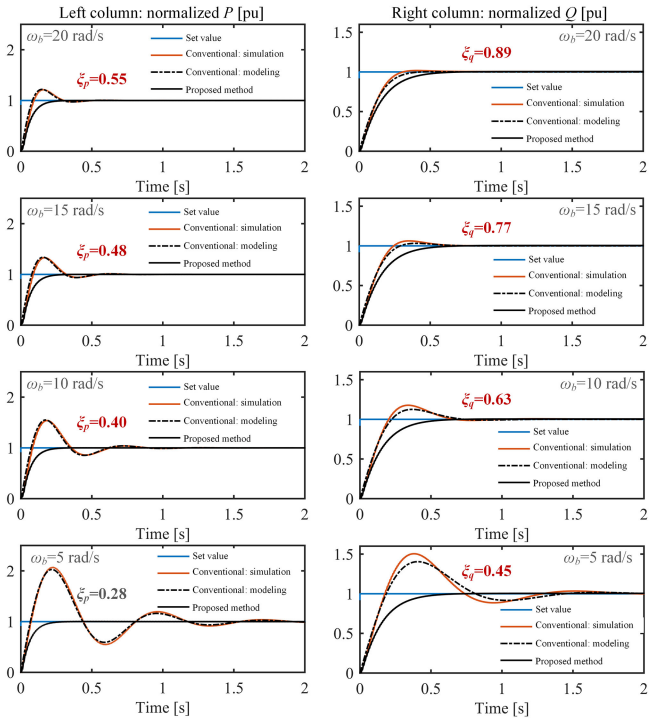

Fig. 15. Simulation results: The variation of ω_b and dynamic response. Left column: Active power response to P_{sel} step change. Right column: Reactive power response to Q_{sel} step change.

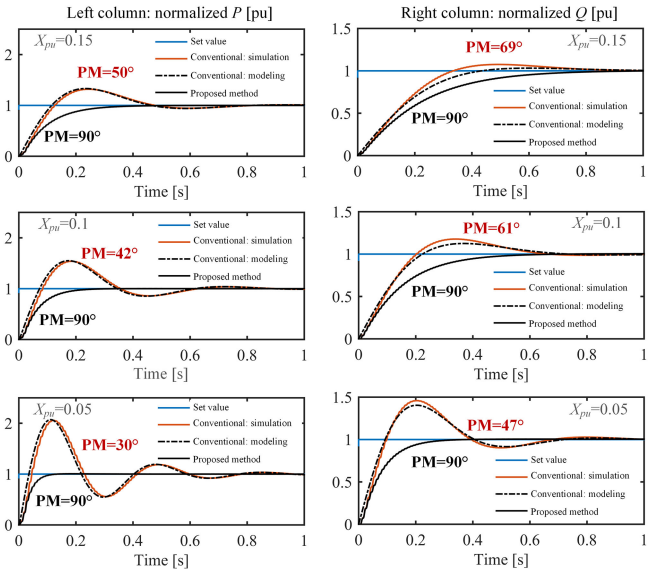

Fig. 16. Simulation results: The variation of X_{pu} and dynamic response. Left column: Active power response to P_{sel} step change. Right column: Reactive power response to Q_{sel} step change.

Fig. 3(b). Two kinds of power regulation controllers are considered, as shown in Figs. 2 (corresponding to the waveform denoted as conventional: simulation) and 9 (corresponding to the waveform denoted as proposed method), respectively. The small-signal modeling result is obtained via the Simulink with the block diagrams in Fig. 6, corresponding to the waveform denoted as conventional: modeling.

The time sequence is given as follows. Before $t = 0$ s, the converter connects to v_g through circuit breaker CB, the converter provides 0 W active power and 0 Var reactive power; at $t = 0$ s, the disturbance comes from two aspects are considered: P_{sel} change and Q_{sel} change. The left columns of Figs. 15 and 16 show the normalized active power P responses to the P_{sel} varies from 0 to 100 W; The right columns of Figs. 15 and 16 show the normalized reactive power Q responses to the Q_{sel} varies from 0 to 100 Var.

1) Dynamic Response and the Variation of APC Bandwidth: The first simulation will demonstrate the dynamic response change under the variation of APC bandwidth ω_b. Fig. 15 shows the dynamic response of output active/reactive power P and Q, corresponding to different values of damping ratios ξ_p, ξ_q. The per-unit ac-side reactance is $X_{\text{pu}} = 0.1$ ensuring variable consistency in the comparison.

For VSC controlled with the conventional power regulation controller, the simulation results coincide with the small-signal results quite well, hence, the damping ratio (32) and (33), obtained from the small-signal model, can be used to describe the dynamic oscillation issue. From $\omega_b = 20$ to $\omega_b = 5$, the damping ratios change from $\xi_p = 0.55, \xi_q = 0.89$ to $\xi_p = 0.28, \xi_q = 0.45$. The decreasing of damping ratios intensifies the dynamic oscillation. When $\xi_p = 0.28$, the overshoot in P is 100%. When $\xi_q = 0.45$, the overshoot in Q is 50%. However, VSC controlled with the proposed power regulation controller does not have the

TABLE II
PARAMETERS OF THE THREE-PHASE VSC

Parameters	Values	Parameters	Values
τ_f	0.001s	τ_v	0.005 s
α	2 %	β	10 %
V_{DC}	700 V	Nominal voltage	220 V
Nominal frequency	50 Hz	Nominal apparent power	3 kVA

dynamic oscillation issue, this fact coincide with the analysis discussed previously. Thus, with the proposed power regulation controller, VSC obtains a better robustness when APC bandwidth changes.

2) Dynamic Response and the Variation of AC-Side Reactance: The second simulation will demonstrate the dynamic response change under the variation of ac-side reactance. The result uses its per-unit value X_{pu}, ensuring the general applicability. Fig. 16 shows the dynamic response of output active/reactive power P and Q, with different values of per-unit ac-side reactance X_{pu}. The APC bandwidth is $\omega_b = 10$ for variable consistency in the comparison.

For the VSC controlled with the conventional power regulation controller, following with the decrease of X_{pu}, the phase margin PM decreases. Although the system is still stable, the overshoot increases following with the decrease of X_{pu}. The peak of active power can be as large as 100%, and the peak of reactive power can be as large as 50%. However, the disturbance creates no overshoot in VSC controlled with the proposed power regulation controller, the phase margin is always 90°, no matter how X_{pu} changes. Thus, with the proposed power regulation controller, VSC obtains a better robustness when ac-side reactance changes.

B. Three-Phase System

A three-phase VSC simulation is given in this part to further demonstrate the proposed controller. The simulation is carried out in MATLAB R2014b with Simulink. The solver used in the simulation was ode23tb with a relative tolerance of 10^{-3} and a maximum step size of 0.2 ms. The power part is shown in Fig. 3(a). Two kinds of power regulation controllers are considered, as shown in Figs. 2 (corresponding to the waveform denoted as conventional controller) and 9 (corresponding to the waveform denoted as proposed controller), respectively. Fig. 17 shows the waveforms ofω, P, V_o, and Q. The left column gives the waveform from a three-phase grid-connected VSC controlled by the conventional method, whereas the right column gives the counterpart controlled by the proposed method.

The time sequence is given as follows. Before $t = 1.5$ s, the converter connects to v_g through circuit breaker CB, the converter provides 1.5 kW active power and 0 Var reactive power; At $t = 1.5$ s, P_{sel} increases 800 W; At $t = 2.5$ s, Q_{sel} increases 500 Var.

The parameters of the converter used in the simulation is given in Table II. Here, $D_p = 1.52$, which means that a frequency drop of 2% causes the torque (hence, the power) to increase by 100% (from nominal apparent power), i.e., $\alpha = 2\%$. $D_q = 96.42$, which means that a voltage drop of 10% causes

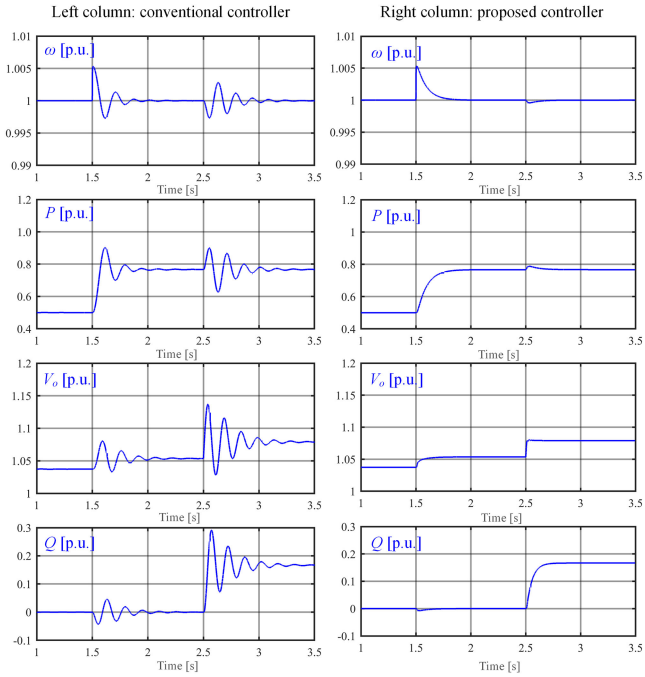

Fig. 17. Dynamic performance comparison. Left column: VSC with conventional controller. Right column: VSC with the proposed controller.

the reactive power to increase by 100% (from nominal apparent power), i.e., $\beta = 10\%$. Control parameters τ_f and τ_v are designed based on the recommendation in [15].

The VSC with the conventional controller showed large oscillation and overshoot during each dynamic period, after $t = 1.5$ s and $t = 2.5$ s. Meanwhile, the VSC controlled by the proposed method obtained a smooth dynamic response. The controller proposed in this paper is also suitable for VSC in the three-phase system.

V. EXPERIMENT RESULTS

A 100-W single-phase VSC prototype, as shown in Fig. 18, is built to verify the aforementioned ideas. The prototype used the same parameter as the simulation shown in Table I. Then, the controller is realized by a DSP TMS320F28335, where the input signals are sampled with an LEM voltage transducer LV 25-P and an LEM current transducer LA 25-P. The sampling frequency and the power device switching frequency are both 10 kHz. The waveforms are calculated by the DSP, transported by the DSP ePWM module, filtered by high-frequency *RC* filters and measured by the Tektronix oscilloscope DPO3034. The *RC* filter is designed to filter out the switching frequency signals. The time constant is 2.2 ms (with a 220-Ω resistor and a 10-μF capacitor), which is far smaller than the VSC response time, so the *RC* filter will not influence the dynamic experiment results. Two kinds of power regulation controllers are considered, as shown in Figs. 2 (corresponding to the waveform denoted as conventional controller) and 9 (corresponding to the waveform denoted as proposed controller), respectively.

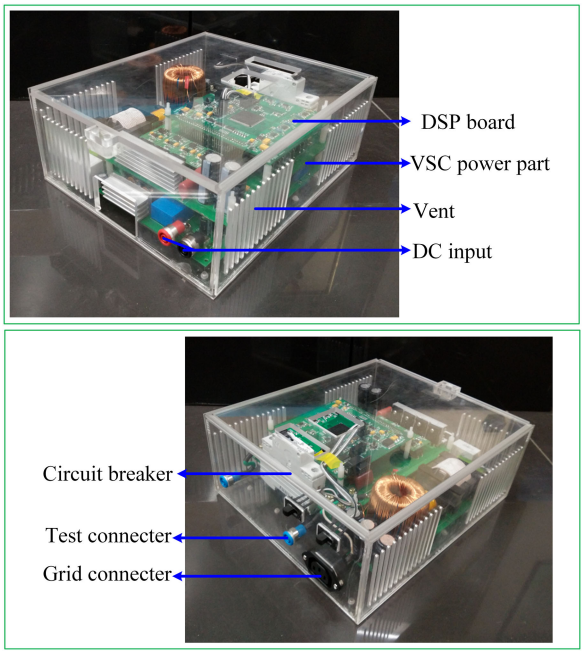

Fig. 18. VSC prototype for experiment.

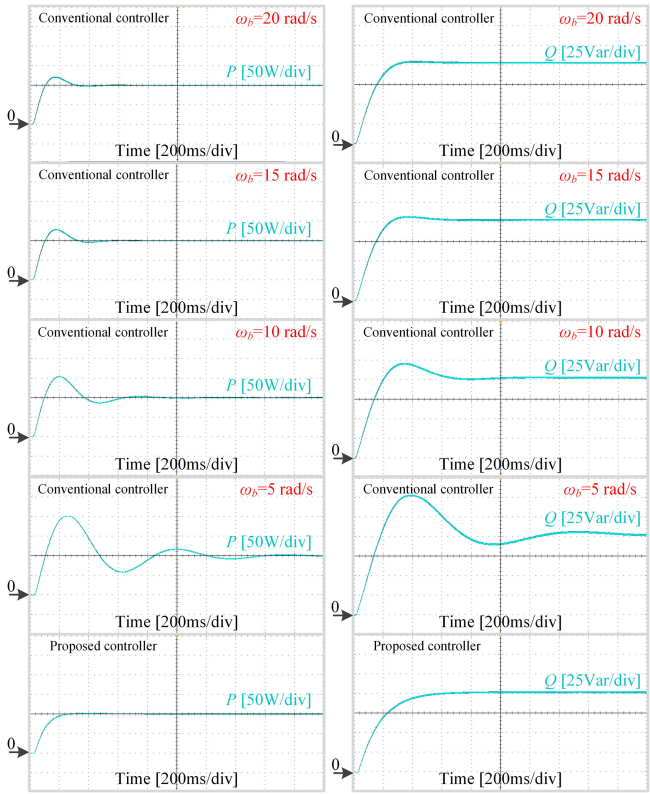

Fig. 19. Experiment results: The variation of ω_b and dynamic response. Left column: Active power response to P_{sel} step change. Right column: Reactive power response to Q_{sel} step change.

A. *Robustness Against Parameter Variation*

This part of experiment corresponds to the simulation section. In order to avoid the damage of power device from the oscillation, this part of experiment uses virtual current for controllers. The current i in the controllers shown in Figs. 2 and 9 is calculated in DSP with the voltage difference: $i = \frac{e - v_g}{Z_s + Z_g}$. At the beginning, the converter output 0 W active power and 0 Var reactive power. The left columns of Figs. 19 and 20(a) show the response of converter active power under the disturbance that P_{sel} changes from 0 to 100 W, whereas the right columns of Figs. 19 and 20(b) show the response of converter reactive power under the disturbance that Q_{sel} changes from 0 to 100 Var.

1) Variation of APC Bandwidth: Fig. 19 shows the experiment results of the VSC with different values of APC bandwidth ω_b. The per-unit ac-side reactance is $X_{\text{pu}} = 0.1$ and the APC bandwidth is $\omega_b = 20, 15, 10, 5$. The experiment results in Fig. 19 coincide with the simulation results in Fig. 15 well.

For the VSC controlled with the conventional power regulation controller, when $\omega_b = 5$, the overshoot in P is 100% and the overshoot in Q is 50%. The increased overshoot is caused by the decrease of damping ratio. However, for the VSC controlled with the proposed power regulation controller, the change of ω_b does not influence the dynamic process. Because it is a first-order system, as given in (35) and (36). The dynamic process is only influenced by τ_p and τ_q, as shown in (24) and (25), and τ_p and τ_q are not influenced by ω_b .

2) Variation of AC-Side Reactance: Fig. 20(a) and (b) shows the active power (P) and reactive power (Q) response to the step change of P_{sel} and Q_{sel}, respectively. The APC bandwidth is $\omega_b = 10$ and the per-unit ac-side reactance is $X_{\text{pu}} = 0.15, 0.1, 0.05$.

For the VSC controlled with the conventional power regulation controller, as shown in the left column of Fig. 20, following with the decrease of X_{pu}, the overshoots increase. The peak of active power can be as large as 100%, and the peak of reactive power can be as large as 50%. However, as it is shown in the right column of Fig. 20, the disturbance creates no overshoot in the response when using the proposed controller, hence, optimizing robustness against the change of ac-side reactance.

B. *Optimized Dynamic Response*

This part of the experiment compares the dynamic response with different controllers. The power part is shown as Fig. 3(b). Fig. 21 gives the waveforms of ω, P, V_o, and Q. At first stage, the converter is connected with the grid by CB. At the start of the second stage, about 2–2.5 s in Fig. 21, P_{sel} changes from 0 to 50 W. At the start of the third stage, about 6.5 –7 s in Fig. 21, Q_{sel} changes from 0 to 50 Var. In this part of experiment, the APC bandwidth $\omega_b = 10$. The grid voltage is realized by the programmable ac source Chroma 61705, with an inner impedance $Z_g = 0.1 + j0.032\ \Omega$. Virtual stator inductor $L_s = 0.65$ mH which corresponds to $X_{\text{pu}} = 0.14$. The filter capacitor $C_f = 44\ \mu F$. V_{DC} is realized by the Chroma 62024P-600-8 programmable dc source. As shown in Fig. 21, by using the proposed controller, the VSC dynamic character is enhanced with reduced overshoots.

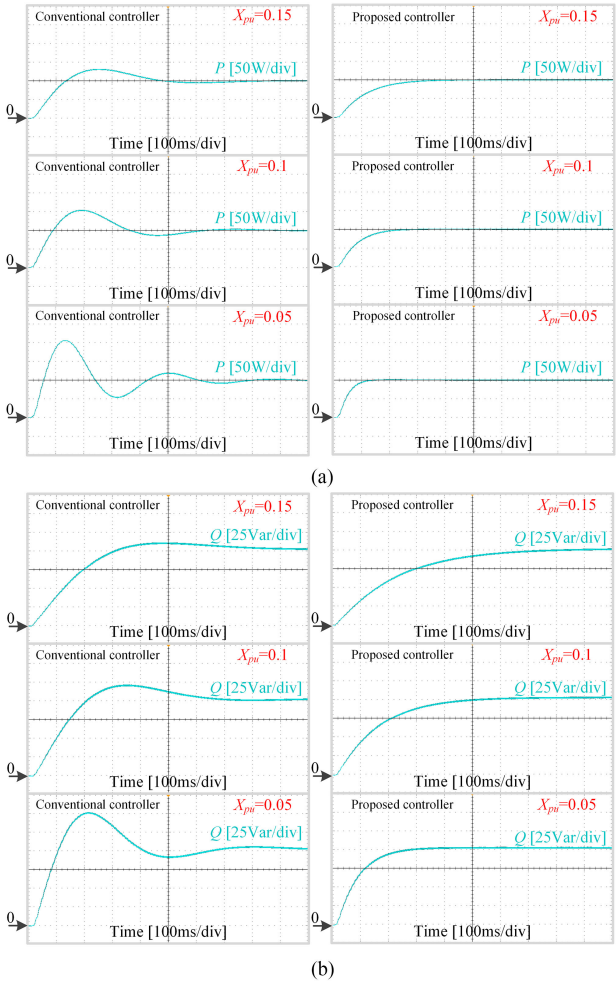

Fig. 20. Experiment results under the variation of X_{pu}. (a) Active power response to P_{sel} step change. (b) Reactive power response to Q_{sel} step change.

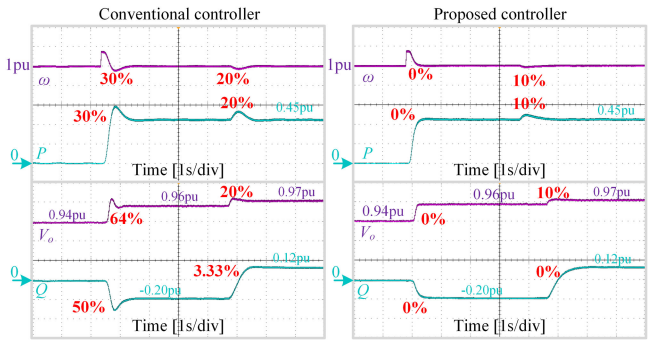

Fig. 21. Experiment results: Overshoot reduction in dynamic response.

VI. Conclusion

Grid-connected VSC might tend to oscillate under parametric uncertainty, treating the safe operation. To enhance the VSC dynamic response and obtain enhanced robustness against parameter variation, this paper proposes an optimized VSC controller with feedforward branch. With the model reduction mechanism, the active/reactive power loops are modified from high-order systems into first-order systems. Hence, the relative stability independent with delay parameters and the VSC dynamic performance is enhanced. Simulation and experiment results show that the dynamic response is significantly smoothed, demonstrating the possibilities of the proposed approach can optimize the VSC dynamic response and robustness against the parameters variation.

References

[1] M. B. Mcelroy and X. Chen, "Wind and solar power in the United States: Status and prospects," *CSEE J. Power Energy Syst.*, vol. 3, no. 1, pp. 1–6, 2017.
[2] C. D. Ahrens, "Transition to very high share of renewables in Germany," *CSEE J. Power Energy Syst.*, vol. 3, no. 1, pp. 17–25, 2017.
[3] P. Pinson, L. Mitridati, C. Ordoudis, and J. Ostergaard, "Towards fully renewable energy systems: Experience and trends in Denmark," *CSEE J. Power Energy Syst.*, vol. 3, no. 1, pp. 26–35, 2017.
[4] Z. Lu, X. Ye, Y. Qiao, and Y. Min, "Initial exploration of wind farm cluster hierarchical coordinated dispatch based on virtual power generator concept," *CSEE J. Power Energy Syst.*, vol. 1, no. 2, pp. 62–67, 2015.
[5] J. Elizondo and J. L. Kirtley, "Effect of inverter-based DG penetration and control in hybrid microgrid dynamics and stability," in *Proc. Power Energy Conf. at Illinois*, Feb. 2014, pp. 1–6.
[6] H. Xie, S. Zheng, and M. Ni, "Microgrid development in China: A method for renewable energy and energy storage capacity configuration in a megawatt-level isolated microgrid," *IEEE Electrific. Mag.*, vol. 5, no. 2, pp. 28–35, Jun. 2017.
[7] N. Pogaku, M. Prodanovic, and T. C. Green, "Modeling, analysis, and testing of autonomous operation of an inverter-based microgrid," *IEEE Trans. Power Electron.*, vol. 22, no. 2, pp. 613–625, Mar. 2007.
[8] Q.-C. Zhong and T. Hornik, *Control of Power Inverters in Renewable Energy and Smart Grid Integration*. Hoboken, NJ, USA: Wiley, 2013.
[9] J. C. Vasquez, J. M. Guerrero, A. Luna, P. Rodriguez, and R. Teodorescu, "Adaptive droop control applied to voltage-source inverters operating in grid-connected and islanded modes," *IEEE Trans. Ind. Electron.*, vol. 56, no. 10, pp. 4088–4096, Oct. 2009.
[10] J. Rocabert, A. Luna, F. Blaabjerg, and P. Rodrguez, "Control of power converters in AC microgrids," *IEEE Trans. Power Electron.*, vol. 27, no. 11, pp. 4734–4749, Nov. 2012.
[11] E. A. Alves Coelho, P. C. Cortizo, and P. F. D. Garcia, "Small signal stability for single phase inverter connected to stiff AC system," in *Proc. 34th IAS Meeting. Conf. Rec. Ind. Appl. Conf.*, 1999, vol. 4, pp. 2180–2187.
[12] J. M. Guerrero, L. G. de Vicuna, J. Matas, M. Castilla, and J. Miret, "A wireless controller to enhance dynamic performance of parallel inverters in distributed generation systems," *IEEE Trans. Power Electron.*, vol. 19, no. 5, pp. 1205–1213, Sep. 2004.
[13] J. M. Guerrero, J. Matas, L. G. de Vicuna, M. Castilla, and J. Miret, "Wireless-control strategy for parallel operation of distributed-generation inverters," *IEEE Trans. Ind. Electron.*, vol. 53, no. 5, pp. 1461–1470, Oct. 2006.
[14] J. Elizondo and J. L. Kirtley, "Effect of dg and induction motor load power rating on microgrid transient behavior," in *Proc. IEEE PES Innov. Smart Grid Technol. Conf.*, 2014, pp. 1–5.
[15] Q.-C. Zhong and G. Weiss, "Synchronverters: Inverters that mimic synchronous generators," *IEEE Trans. Ind. Electron.*, vol. 58, no. 4, pp. 1259–1267, Apr. 2011.
[16] Q. C. Zhong and P. L. Nguyen, "Sinusoid-locked loops based on the principles of synchronous machines," in *Proc. 24th Chin. Control Decis. Conf.*, May 2012, pp. 1518–1523.
[17] Z. Ma, Q.-C. Zhong, and J. Yan, "Synchronverter-based control strategies for three-phase PWM rectifiers," in *Proc. 7th IEEE Conf. Ind. Electron. Appl.*, Singapore, Jul. 2012, pp. 225–230.
[18] T. Shao, T. Q. Zheng, H. Li, and X. Zhang, "Parameter design and hot seamless transfer of single-phase synchronverter," *Elect. Power Syst. Res.*, vol. 160, pp. 63–70, 2018.
[19] P.-L. Nguyen, Q.-C. Zhong, F. Blaabjerg, and J. Guerrero, "Synchronverter-based operation of STATCOM to mimic synchronous condensers," in *Proc. 7th IEEE Conf. Ind. Electron. Appl.*, Singapore, Jul. 2012, pp. 942–947.
[20] W. Long Ming and Q.-C. Zhong, "Synchronverter-based transformerless PV inverters," in *Proc. 40th Annu. Conf. IEEE Ind. Electron. Soc.*, 2014, pp. 4396–4401.

[21] R. Aouini, B. Marinescu, K. B. Kilani, and M. Elleuch, "Synchronverter-based emulation and control of HVDC transmission," *IEEE Trans. Power Syst.*, vol. 31, no. 1, pp. 278–286, Jan. 2016.

[22] S. Dong, Y. N. Chi, and L. Yan, "Active voltage feedback control for hybrid multiterminal HVDC system adopting improved synchronverters," *IEEE Trans. Power Del.*, vol. 31, no. 2, pp. 445–455, Apr. 2016.

[23] S. Dong and Y. C. Chen, "A method to directly compute synchronverter parameters for desired dynamic response," *IEEE Trans. Energy Convers.*, vol. 33, no. 2, pp. 814–825, Jun. 2018.

[24] E. Van Emmerik, B. Franca, and M. Aredes, "A synchronverter to damp electromechanical oscillations in the Brazilian transmission grid," in *Proc. IEEE 24th Int. Symp. Ind. Electron.*, 2015, pp. 221–226.

[25] J. Liu, Y. Miura, and T. Ise, "Power quality improvement of microgrids by virtual synchronous generator control," in *Proc. Elect. Power Qual. Supply Rel.*, Aug. 2016, pp. 119–124.

[26] A. D'Arco and J. R. Suul, "Equivalence of virtual synchronous machines and frequency-droops for converter-based microgrids," *IEEE Trans. Smart Grid*, vol. 5, no. 1, pp. 394–395, Jan. 2014.

[27] R. Aouini, K. B. Kilani, B. Marinescu, and M. Elleuch, "Virtual synchronous generators dynamic performances," in *Proc. Int. Conf. Elect. Sci. Technol. Maghreb*, 2015, pp. 1–6.

[28] S. Dong and Y. C. Chen, "Adjusting synchronverter dynamic response speed via damping correction loop," *IEEE Trans. Energy Convers.*, vol. 32, no. 2, pp. 608–619, Jun. 2017.

[29] L. Zhang, F. Wang, H. Guo, X. Feng, Y. Du, and J. Su, "Perturbation influences of parameters on dynamic performance of a virtual synchronous generator," in *Proc. Conf. IEEE Ind. Electron. Soc.*, 2017, pp. 1405–1410.

[30] S. D'Arco and J. A. Suul, "Virtual synchronous machines-classification of implementations and analysis of equivalence to droop controllers for microgrids," in *Proc. IEEE Grenoble PowerTech*, 2013, pp. 1–7.

[31] H. Wu, X. Ruan, D. Yang, X. Chen, W. Zhao, Z. Lv, and Q. C. Zhong, "Small-signal modeling and parameters design for virtual synchronous generators," *IEEE Trans. Ind. Electron.*, vol. 63, no. 7, pp. 4292–4303, Jul. 2016.

[32] H. Akagi, E. Watanabe, and M. Aredes, *Instantaneous Power Theory and Applications to Power Conditioning*. Hoboken, NJ. USA: Wiley, 2007.

[33] K. Ogata, *Modern Control Engineering*, 3rd ed. Englewood Cliffs, NJ, USA: Prentice-Hall, 1996.

[34] P. S. Kundur, *Power System Stability and Control*. New York, NY, USA: McGraw-Hill, 1994.

[35] A. R. Bergen, *Power Systems Analysis*. Englewood Cliffs, NJ, USA: Prentice-Hall, 1996.

[36] J. M. Guerrero, L. G. de Vicuna, J. Matas, M. Castilla, and J. Miret, "Output impedance design of parallel-connected UPS inverters with wireless load-sharing control," *IEEE Trans. Ind. Electron.*, vol. 52, no. 4, pp. 1126–1135, Aug. 2005.

[37] R. Erickson and D. Maksimović, *Fundamentals of Power Electronics*. Norwell, MA, USA: Kluwer, 2001.

[38] Q. C. Zhong, P. L. Nguyen, Z. Ma, and W. Sheng, "Self-synchronized synchronverters: Inverters without a dedicated synchronization unit," *IEEE Trans. Power Electron.*, vol. 29, no. 2, pp. 617–630, Feb. 2014.

[39] Z. Zheng, W. Shao, L. I. Hui, R. Li, and Q. Song, "Unbalanced voltage control of virtual synchronous generator in islanded micro-grid," *Proc. CSEE*, vol. 37, no. 2, pp. 372–380, 2017.

[40] P. Piya and M. Karimi-Ghartemani, "A stability analysis and efficiency improvement of synchronverter," in *Proc. IEEE Appl. Power Electron. Conf. Expo.*, Mar. 2016, pp. 3165–3171.

[41] K. Padiyar, *Analysis of Subsynchronous Resonance in Power Systems*. Berlin, Germany: Springer Science+Business Media, 2012.

[42] V. Natarajan and G. Weiss, "Synchronverters with better stability due to virtual inductors, virtual capacitors and anti-windup," *IEEE Trans. Ind. Electron.*, vol. 64, no. 7, pp. 5994–6004, Jul. 2017.

[43] J. J. Grainger and W. D. Stevenson, *Power System Analysis*. NewYork, NY, USA: McGraw-Hill, 1994.

[44] L. Shang, H. U. Jiabing, X. Yuan, and Y. Huang, "Improved virtual synchronous control for grid-connected VSCS under grid voltage unbalanced conditions," *J. Mod. Power Syst. Clean Energy*, vol. 7, pp. 174–85, 2018.

[45] C. C. Hua, K. A. Liao, and J. R. Lin, "Parallel operation of inverters for distributed photovoltaic power supply system," in *Proc. Power Electron. Spec. Conf.*, 2002, pp. 1979–1983.

[46] T. Kawabata and S. Higashino, "Parallel operation of voltage source inverters," *IEEE Trans. Ind. Appl.*, vol. 24, no. 2, pp. 281–287, Mar./Apr. 1988.

Tiancong Shao (S'13–M'19) was born in Zibo, Shandong, China, in 1990. He received the B.S. and Ph.D. degrees in electrical engineering from Beijing Jiaotong University, Beijing, China, in 2012 and 2019, respectively.

From 2016 to 2017, he was a Visiting Scholar with the Armour College of Engineering, Illinois Institute of Technology, Chicago, IL, USA. He is currently a Postdoctoral Research Assistant with Beijing Jiaotong University. His current research focuses on power conversion system, including control strategy and the application of wide band-gap semiconductor devices.

Dr. Shao was the recipient of the IEEE International Future Energy Challenge Best Control Design Prize as the Graduate Student Supervisor of Beijing Jiaotong University Representative Team in 2015.

Pengyu Jia was born in Hebei, China. He received the B.S. and Ph.D. degrees in electrical engineering from Beijing Jiaotong University, Beijing, China, in 2008 and 2014, respectively.

From 2014 to 2017, he was with China Academy of Space Technology, Beijing, China. In 2017, he became an Assistant Professor with the College of Electrical and Control Engineering, North China University of Technology, Beijing, China. His current research interests include power electronics converters, stability control, converter modeling technology, and the application of wide band-gap semiconductor devices.

Peiqi Zheng was born in Jiangshan, Zhejiang, China, in 1994. She received the B.S. degree in automation engineering from Zhejiang University City College, Zhejiang, China, in 2016. She is currently working toward the M.S. degree at Beijing Information Science and Technology University, Beijing, China.

Her current research focuses on power electronics, passivity-based control, and multiobjective optimization of power system and renewable energy.

Trillion Q. Zheng (M'06–SM'07) was born in Jiangshan, Zhejiang, China, in 1964. He received the B.S. degree in electrical engineering from Southwest Jiaotong University, Sichuan, China, in 1986, and the M.S. and Ph.D. degrees in electrical engineering from Beijing Jiaotong University, Beijing, China, in 1992 and 2002, respectively.

He is an University Distinguished Professor with Beijing Jiaotong University. He is the Director of the Center for Electric Traction, sponsored by the Ministry of Education, China. His current research interests include the power supplies and ac drives of railway traction systems, high-performance and low loss power electronics systems, and power-quality corrections. He holds 24 Chinese patents and has authored/coauthored more than 80 journal articles and more than 120 technical papers in conference proceedings. From 2003 to 2011, he served as the Dean of the School of Electrical Engineering, Beijing Jiaotong University. He is serving as the Deputy Director of the Beijing Society for Power Electronics.

Dr. Zheng was a Laureate of the Delta Scholar for Power Electronics and Motor Drives of the Delta Environmental and Educational Foundation and received many other provisional-level and national-level awards.

Jiuhe Wang was born in Jilin, China. He received the B.S. degree from the School of Electrical and Control, Liaoning Technical University, Fuxin, China, in 1982, and the Ph.D. degree from the School of Information Engineering, University of Science and Technology Beijing, Beijing, China, in 2005.

He is currently a Professor with the School of Automation, Beijing Information Science and Technology University, Beijing, China. His research interests include nonlinear control of power electronic converter, power quality control, microgrid, etc.

Hong Li (S'07–M'09–SM'18) received the B.Sc. degree from Taiyuan University of Technology, Taiyuan, China, in 2002, the M.Sc. degree from South China University of Technology, Guangzhou, China, in 2005, and the Ph.D. degree from FernUniversität in Hagen, Hagen, Germany, in 2009.

She is currently a Professor with Electrical Engineering School, Beijing Jiaotong University, Beijing, China. She has authored/coauthored one book, 30 journal papers, and 39 conference papers. She has also applied 20 patents. Her research interests include nonlinear modeling, analysis, and its applications, EMI suppressing methods for power electronic systems, wideband gap power devices, and applications.

Prof. Li is an Associate Editor for IEEE TRANSACTIONS ON INDUSTRIAL ELECTRONICS, Associate Editor for the *Chinese Journal of Electrical Engineering*, and Vice-Chairman of Electromagnetic Compatibility Specialized Committee in China Power Supply Society.

Mei Liang was born in Hebei, China, in 1988. She received the B.Sc. and Ph.D. degrees in electronic engineering from Beijing Jiaotong University, Beijing, China, in 2011 and 2018, respectively.

Since 2018, she has been with ABB (China) Ltd., Beijing, China, Cooperate Research Center, as a Scientist. Her research interests include analysis of power electronics converter topologies, efficient switching techniques, and wide bandgap semiconductor applied research.

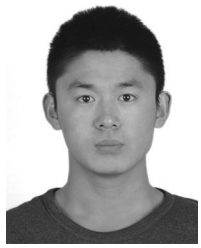

Xiaochao Zhang was born in Shandong, China, in 1992. He received the B.S. degree in electrical engineering from Shandong University of Science and Technology, Shandong, China, in 2016. He is currently working toward the M.S. degree in electrical engineering at the School of Electrical Engineering, Beijing Jiaotong University, Beijing, China.

His research interest includes modeling and control of grid-connected inverter.